RSC Advances

PAPER

View Article Online
View Journal | View Issue

Cite this: *RSC Adv.*, 2025, **15**, 5327

High-precision optical thermometry using Pr^{3+}-doped $NaCaY(MoO_4)_3$ luminophores: a multi-spectral and chromaticity-based approach to non-contact temperature sensing†

Zein El Abidine Aly Taleb, Kamel Saidi and Mohamed Dammak *

A series of $NaCaY(MoO_4)_3$ (NCYM) phosphors doped with Pr^{3+} ions was synthesized to develop advanced materials for optical temperature sensing. The structures, morphologies, and luminescent characteristics of these phosphors were thoroughly analyzed. X-ray diffraction (XRD) results confirm that all phosphors exhibit a tetragonal phase with a scheelite-type structure. Optical properties were characterized using UV-visible absorption and photoluminescence (PL) spectroscopy. Under 450 nm excitation, optimal luminescence intensity was achieved at a Pr^{3+} concentration of 30 mol%. Fluorescence intensity ratio (FIR) techniques, based on emissions from various excited states of Pr^{3+} ($^3P_1 \rightarrow {}^3H_5$ and $^3P_0 \rightarrow {}^3H_5$; $^3P_1 \rightarrow {}^3H_5$ and $^3P_0 \rightarrow {}^3F_2$), were employed for thermometric characterization over the 298–498 K range. The results indicate excellent temperature detection performance, with maximum relative sensitivities of 0.69% per K and 1.2% per K at 298 K, respectively. Additionally, a study of temperature uncertainty (δT) demonstrated values below 0.06 K, with repeatability (R) exceeding 97%. The temperature-induced shift in chromaticity further improves the material's functionality, as the CIE coordinates change from (0.3806, 0.4278) at 298 K to (0.3772, 0.4229) at 498 K, demonstrating a stable transition towards yellow. These findings suggest that Pr^{3+}-activated NCYM phosphors have significant potential for application in non-contact optical thermometry.

Received 5th January 2025
Accepted 13th February 2025

DOI: 10.1039/d5ra00093a

rsc.li/rsc-advances

1. Introduction

Temperature is a fundamental physical parameter that holds a pivotal role across diverse domains, including scientific research, engineering, and industrial applications. In recent decades, luminescent materials have emerged as an innovative solution to the inherent limitations of traditional contact thermometers.[1,2] These remote temperature measurement systems have been extensively explored and applied in numerous fields, offering distinct advantages. One key benefit of optical thermometry is its exceptional accuracy, which is crucial in precision-demanding applications such as semiconductor manufacturing, food safety monitoring, and medical diagnostics.[3,4] Moreover, optical thermometers are particularly advantageous in extreme environments where contact-based methods are impractical, such as high-temperature or corrosive conditions.[5] Recent technological advancements have further refined the precision of optical thermometry, making it an increasingly preferred option for a wide range of applications.[6] Among the various approaches, the fluorescence intensity ratio (FIR) technique in phosphor materials has garnered significant attention. This method is extensively studied for its advantages, including non-contact measurement, rapid response times, and high spatial and temporal resolution, enabling effective temperature detection in challenging conditions or for rapidly moving objects.[7,8] In FIR thermometry, two distinct emission peaks serve as reference signals. The efficacy of FIR-based thermometric materials is defined by three critical parameters: high absolute temperature sensitivity (S_a), high relative temperature sensitivity (S_r), and excellent signal discriminability.[9,10] Rare-earth ions are highly suitable for temperature sensing due to their unique optical properties, which include sharp emission bands, narrow linewidths, long lifetimes, and high quantum efficiencies. These features make them highly responsive to temperature variations. Most studies in this field focus on thermally coupled level pairs (TCLs) of rare-earth ions, such as the $^2H_{11/2}$ and $^4S_{3/2}$ levels of Er^{3+}, the $^3F_{2,3}$ and $^3H_4$ levels of Tm^{3+}, and the $^4F_{7/2}$ and $^4F_{3/2}$ levels of Nd^{3+}.[11–15] In these systems, the populations of the upper and lower TCLs exhibit an inverse relationship as temperature increases, leading to variations in the fluorescence intensity ratio (FIR).

The energy gap between TCLs significantly impacts thermometric performance. A narrow gap enhances absolute

Laboratoire de Physique Appliquée, Groupe des Matériaux Luminescents, Faculté des Sciences de Sfax, Département de Physique, Université de Sfax, Sfax, BP 1171, Tunisia. E-mail: madidammak@yahoo.fr; Mohamed.dammak@fss.usf.tn

† Electronic supplementary information (ESI) available. See DOI: https://doi.org/10.1039/d5ra00093a

temperature sensitivity (S_a) but compromises relative sensitivity (S_r) and signal discriminability due to overlapping emission peaks. Conversely, a wider energy gap improves Sr and signal discriminability but reduces thermal coupling, leading to a lower S_a.[16,17] Consequently, achieving simultaneous optimization of S_a, S_r, and signal discriminability remains a challenge in TCL-based optical thermometry. In addition, the selection of host materials is a critical factor in designing effective optical sensors, as it influences the overall performance and suitability of the thermometric system.

In this study, we propose a highly sensitive and precise method for monitoring elevated temperatures, up to approximately 498 K, utilizing a newly developed Pr^{3+}-doped NCYM phosphor. Molybdates, represented by the general formula $NaCaY(MoO_4)_3$ (NCYM), stand out for several reasons. These materials exhibit broad, intense absorption bands in the near-UV region, mainly attributed to charge transfer (CT) transitions. Among the various molybdate compounds, NCYM was chosen for its stable physical and chemical properties, as well as its particularly low phonon energy, and can accommodate higher concentrations of rare earth ions.

This material is not only cost-effective but also straightforward to synthesize, exhibiting broad and intense absorption bands in the near-UV region, primarily attributed to charge transfer transitions (CTB). The molybdate host matrix serves as an excellent platform due to its stable chemical properties, low phonon energy, and the ability to accommodate high concentrations of rare-earth ions. These attributes, combined with the crystal structure and luminescent characteristics of Pr^{3+}-activated NCYM phosphors, make them highly suitable for temperature sensing applications. To characterize its thermometric properties, we examined the thermal responses of Pr^{3+} emissions over the temperature range of 298–498 K, focusing on specific transitions: ($^3P_1 \rightarrow {}^3H_5$ and $^3P_0 \rightarrow {}^3H_5$) and ($^3P_1 \rightarrow {}^3H_4$ and $^3P_0 \rightarrow {}^3F_2$). The temperature sensor's performance was evaluated using three fluorescence intensity ratio (FIR)-based optical thermometry models, which demonstrated high sensitivity and consistent reliability in temperature measurement.

2. Experimental

2.1. Materials

In this study, all chemical reagents were obtained from Sigma-Aldrich and used without additional purification. $NaCaY(MoO_4)_3$:xPr^{3+} phosphor samples (x = 0.1, 0.2, 0.3, and 0.4) were synthesized using a citrate-based sol–gel method. The raw materials included sodium nitrate [($Na(NO_3)_3$, 99.0%)], calcium nitrate tetrahydrate [($Ca(NO_3)_2 \cdot 4H_2O$, 99.0%)], yttrium(III) nitrate hexahydrate [($Y(NO_3)_3 \cdot 6H_2O$, 99.9%)], praseodymium(III) nitrate hexahydrate [($Pr(NO_3)_3 \cdot 6H_2O$, 99.9%)], ammonium molybdate tetrahydrate [($(NH_4)_6Mo_7O_{24} \cdot 4H_2O$, 99.9%)], and citric acid [$C_6H_8O_7$, 99.0%].

2.2. Synthesis procedure

At the outset of the synthesis process, stoichiometric amounts of sodium nitrate, calcium nitrate tetrahydrate, yttrium nitrate hexahydrate, praseodymium nitrate hexahydrate, and ammonium molybdate tetrahydrate were dissolved in 200 mL of deionized water. To this solution, 5 moles of citric acid were added as a chelating agent, ensuring a citric acid-to-metal ion ratio of 1 : 2. This process produced a total of 1.5 g of the final product. The solution was stirred at room temperature for one hour to ensure homogeneity. Upon heating, the initially transparent solution gradually turned blue, eventually forming a blue wet gel. The container was then left uncovered to facilitate liquid evaporation. The resultant blue gel was dried at 423 K for 12 hours in an oven, producing a xerogel—a stable, porous matrix. This xerogel was subsequently annealed at 673 K for 3 hours, yielding black particles. Finally, the sample underwent sintering in air at 973 K for 3 hours, resulting in pure-phase crystalline particles.

3. Characterizations techniques

The characterization of the synthesized samples involved multiple analytical techniques. X-ray powder diffraction (PXRD) patterns were recorded at room temperature using a Bruker D8-Advance diffractometer with CuKα_1 radiation (λ = 1.5406 Å) 20°–80° 2θ degrees. The morphology of the samples was examined using a Zeiss Supra55VP field-emission scanning electron microscope (FEG-SEM), equipped with a Bruker XFlash 5030 detector for enhanced imaging resolution. UV-vis-NIR absorption spectra were acquired using a PerkinElmer Lambda 365 spectrometer. For photoluminescence (PL) characterization, excitation spectra were measured with a Horiba Fluoromax 4P spectrometer, utilizing a xenon lamp as the excitation source at room temperature. The absolute quantum (QY) yield was determined by the integrating sphere method on the HORIBA JOBIN YVON Fluoromax-4 spectrofluorometer. An Easy Life-Horiba instrument was employed to measure the emission lifetime. The light source was a 450 nm diode laser. The optical thermometry study was conducted in a custom-built nanometric-heating chamber, ensuring temperature control accuracy within ±0.5 K. Emission spectra were recorded under excitation by a 450 nm diode laser operating at a constant power of 30 mW. A Horiba Jobin Yvon iHR320 monochromator spectrometer, equipped with an 1800 lines per mm grating optimized for 500 nm, was used for spectral analysis. A Hamamatsu R928 photomultiplier tube detected luminescence across the blue, green, and red emission bands. Sample temperatures were systematically varied from room temperature to 498 K in 10 K increments.

4. Results and discussion

4.1. X-ray diffraction analysis

X-ray diffraction (XRD) patterns were employed to examine the crystal structure and phase purity of the NSGM:xPr^{3+} microcrystals (where x = 0.1, 0.2, 0.3, and 0.4). Fig. 1(a) displays the XRD patterns of these samples in the 20–80° 2θ range. All observed diffraction peaks are indexed to a pure scheelite-type tetragonal structure with the space group $I4_1/a$, consistent with the Joint Committee on Powder Diffraction Standards

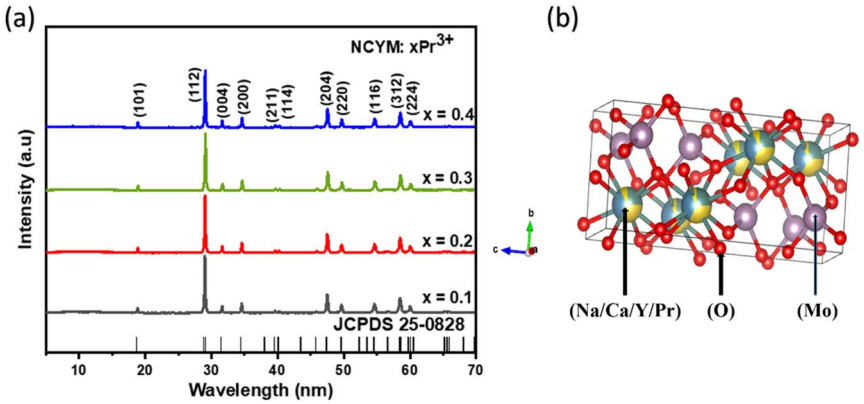

Fig. 1 (a) XRD of the NCYM:xPr^{3+} (x = 0.1, 0.2, 0.3 and 0.4), (b) crystal structure of NCYM.

(JCPDS) pattern no. 25-0828. The absence of impurity peaks confirms that the Pr^{3+} ions were successfully incorporated into the Y^{3+} sites, resulting in the intended pure molybdate structure. In order to confirm the crystal structure, the structural parameters of NCYM:xPr^{3+} were refined using the Rietveld method (Fig. S_1(a–d)†). The diffraction peaks show good agreement between the observed and calculated patterns. The refined lattice parameters, cell volume, and structural details are provided in Table S_1,† which further reinforce the structural integrity of the synthesized material. Fig. 1(b) illustrates the of NCYM doped with Pr^{3+} and the coordination of Na/Ca/Y/Pr and Mo coordination. Given the similar ionic radii of Y^{3+} (1.019 Å, C. N. = 8) and Pr^{3+} (1.126 Å, C. N. = 8),[18,19] the Pr^{3+} ions are most likely to replace Y^{3+} ions and occupy the Y positions. The radius percentage difference (D_r) between the potential substituted ions and dopants is calculated using the following equation:[20]

$$D_r = \frac{R_S - R_D}{R_S} \times 100 \quad (1)$$

where R_S and R_D refer to the effective ionic radii of substituted cations and dopants, respectively. In our work, the D_r value between Y^{3+} and Pr^{3+} is about 9.5%, which is less than 30%, indicating that Pr^{3+} ions can be substituted for Y^{3+} ions.

4.2. Morphology characterization

The scanning electron microscope (SEM) technique was utilized to explore the surface morphology and grain size distribution. The SEM images of NCYM:xPr^{3+} samples are shown in Fig. 2(a–d). It is evident that the irregular shapes result from the aggregation of grains and are on the micrometer scale, which is favorable for improving their photoluminescence (PL) properties.

4.3. Optical characterization

4.3.1. UV absorption spectroscopy. Fig. 3(a–d) presents the UV-vis DR spectra for the NCYM:xPr^{3+} samples (x = 0.1, 0.2, 0.3, and 0.4). A prominent absorption band is observed in the near-ultraviolet (NUV) region, extending from 200 to 800 nm, which is attributed to the charge transfer band (CTB) of Mo–O. Furthermore, additional absorption peaks at 452, 475, 490, and 600 nm correspond to the $^3H_4 \rightarrow {}^3P_2$, $^3P_1$, $^3P_0$, and $^3H_4 \rightarrow {}^1D_2$ electronic transitions, respectively.[21,22]

The plots of $[F(R_\infty)h\nu]^2$ *versus* photon energy ($h\nu$) for NCYM:xPr^{3+} (x = 0.1, 0.2, 0.3 and 0.4) are shown in Fig. S_2(a–d),† the direct optical band gap values (E_g) can be obtained by using K–M function and Tauc formulae:[23,24]

$$F(R_\infty) = \frac{(1 - R_\infty)^2}{2R_\infty} = \frac{K}{S} \quad (2)$$

$$[F(R_\infty)h\nu] = B(h\nu - E_g)^n \quad (3)$$

where R_∞ was the ratio of the light scattered from the sample and $F(R_\infty)$ was K–M function; S was scattering coefficient; K was absorption coefficient; $h\nu$ was the photon energy, E_g was the bandgap energy and n is a parameter that defines the nature of the band transition. The value of n is 1/2 for direct allowed transitions and 2 for indirect allowed transitions. Previous studies have confirmed that NCYM is a direct bandgap material. The optical bandgap values for the NCYM:xPr^{3+} samples (x = 0.1, 0.2, 0.3, and 0.4) fall within the range of 3.36 to 3.84 eV,

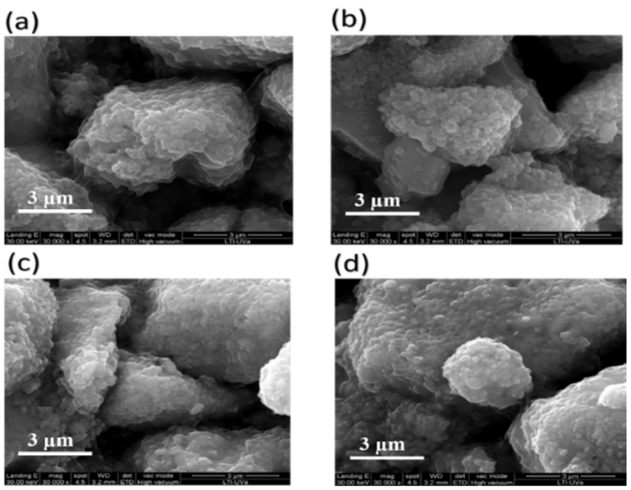

Fig. 2 SEM microscopic morphology image of NCYM:xPr^{3+} (x = 0.1 (a), 0.2 (b), 0.3 (c) and 0.4 (d)).

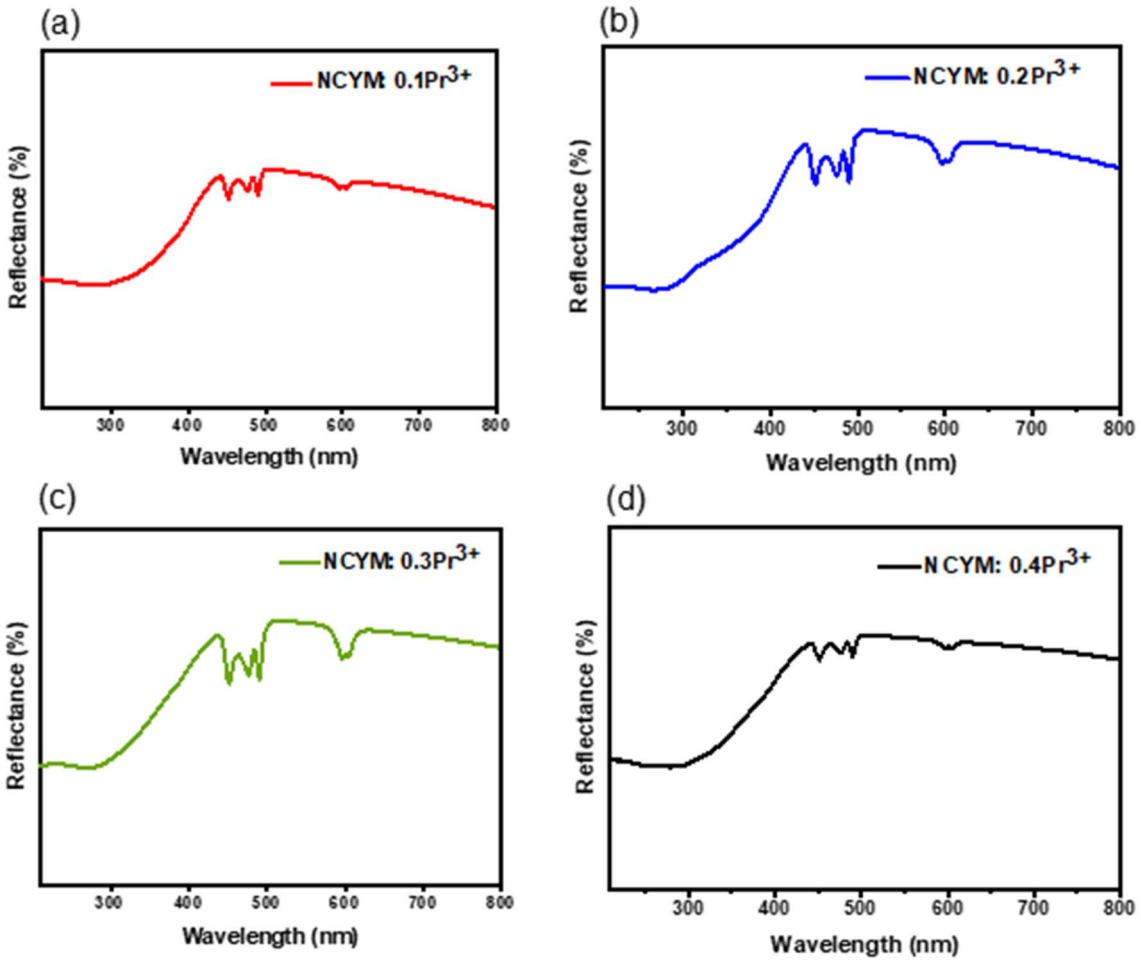

Fig. 3 (a–d) Diffuse reflectance spectra of the NCYM:xPr^{3+} (x = 0.1, 0.2, 0.3 and 0.4).

demonstrating that the incorporation of Pr^{3+} ions have minimal influence on the band gap values.

4.3.2. Photoluminescence properties. The room temperature PLE and PL spectra of NCYM:Pr^{3+} phosphor are shown in Fig. S$_3$† and 4(a), respectively. PLE spectrum, with an excitation wavelength of 650 nm exhibit a broad band in the UV range and a series of sharp lines in the visible range, which are in accordance with the results in UV-vis diffuse reflectance spectra (Fig. 3). The PL of the NCYM:0.3Pr^{3+} sample at the monitoring wavelength of 450 nm is shown in Fig. 4(a). Several prominent peaks are observed, including tow cyan emissions at 490 nm and 500 nm, two green emissions at 533 nm and 558 nm, as well as intense red emissions at 621 nm and 651 nm. Additionally, several weaker red emissions are detected at 602 nm, 628 nm, 692 nm, 712 nm, and 735 nm. The $^3P_0$ state is populated *via* optical excitation, leading to electronic transitions that are followed by a non-radiative mechanism. The radiative depopulation of the $^3P_0$ state gives rise to multiple emission bands in the red region of the spectrum, including transitions from $^3P_0 \rightarrow {}^3H_6$ (with a maximum at 621 nm), $^3P_0 \rightarrow 3F_2$ (at 651 nm), and $^3P_0 \rightarrow {}^3F_4$ (at 736 nm). It is noteworthy that the emission characteristics of Pr^{3+} in NCYM are host-dependent; in certain hosts, Pr^{3+} favors a strong $^1D_2 \rightarrow {}^3H_4$ transition with weak or even negligible emission from the $^3P_0$ state.[25,26] On the other hand, when excitation by a laser diode by energy matched to the $^3P_2$ praseodymium level, non-radiative transition of the excitation energy to the $^3P_0$ and $^1D_2$ emitting levels occurs. Then, the emission from these levels to the ground state $^3H_4$ and higher excited states take place. The observed luminescence is also quenched by a non-radiative cross-relaxation process that occurs in ion pairs when ions are close enough to each other according to the following schemes: $[{}^1D_2, {}^3H_4] \rightarrow [{}^1G_4, {}^3F_4]$. When excited in the $^3P_2$ band, the energy is transferred non-radioactively to the nearby $^3P_0$ level, from which luminescence occurs. On the other hand, the emission from the $^1D_2$ level can be populated from the $^3P_0$ level by multi-phonon relaxation due to the high energy of the phonons in the molybdate matrices of around 900 cm^{-1}.[27]

The energy bandgap law states that if the difference between two energy levels is greater than five times the value of the highest energy phonon in the host medium, the probability of multiphonon relaxation will be negligible. The multiphonon non-radiative transition rates "W_{NR}" can be written using the formula:[28,29]

$$W_{NR} = (1/t_0)\exp(-ap) \quad (4)$$

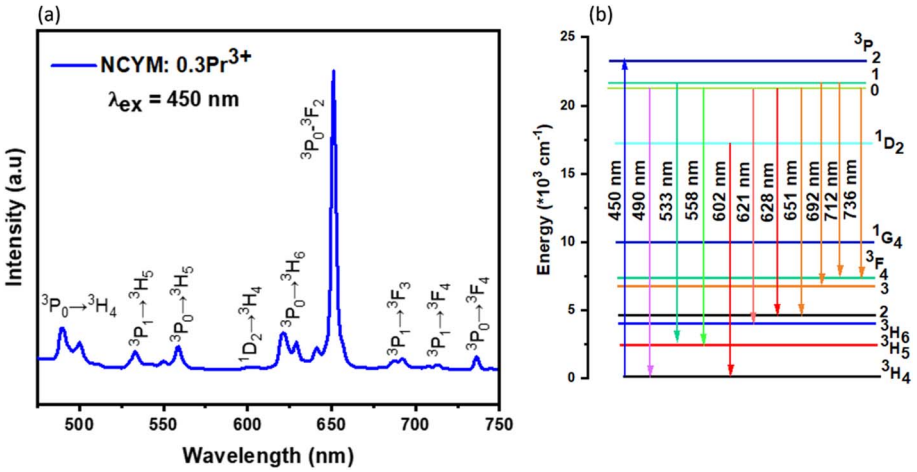

Fig. 4 (a) PL spectrum of NCYM:0.3Pr^{3+} excited by 450 nm; (b) the schematic of the energy levels of Pr^{3+} ions and the possible transitions when excited by 450 nm.

where $p = \Delta E/h\nu_{max}$ is the number of phonons needed to overcome the ΔE gap, h is the Planck constant, ν_{max} is the highest phonon frequency in the host, and t_0 and a are the empirically fitted parameters. The absorption spectrum shows that the energy distance between the $^3P_0$ and $^1D_2$ levels is less than 3000 cm^{-1}; therefore, in the case of this host as well as other molybdate, since $p \approx 3$, the probability of multiphonon relaxation will be significant. The cross-relaxation process [$^3P_0$, $^3H_4$] → [$^3H_6$, $^1D_2$] could also populate the $^1D_2$ level but is much weaker than those from $^1D_2$ because, according to the selection rule, they are spin-forbidden. The multiphonon relaxations taking place between $^1D_2$ and $^1G_4$ state can be ignored, as they need at least 7 to 8 phonons to bridge the large energy gap (9982 cm^{-1}). Therefore, the involvement of multiphonon relaxations cannot be completely neglected in case of emission from $^3P_0$. This suggests that, depopulation of $^3P_0$ state takes place very fast through multi phonon relaxations by feeding the $^1D_2$ state, and also W_{MPR} has negligible influence on the depopulation of this state resulting in high emission efficiency at lower concentration (0.5 mol%). In other words non-radiative multiphonon relaxations from the $^3P_{0,1}$ states at lower concentrations (≤0.005) favours the emission from $^1D_2$ state to be more dominant, while at higher concentrations (≥0.005 mol) the energy transfer process becomes efficient and fast quenching in emission intensity takes place through cross relaxations due to enhanced nonradiative coupling between ions. Based on this discussion, the multiphonon relaxation rates along with cross relaxations favours the depopulation of $^3P_0$ state while multiphonon relaxations can be neglected in case of $^1D_2$ state. Hence, cross relaxations could play a major role in the trends observed in emission spectra emission from $^1D_2$ state with respect to ion concentration.[30–33]

The 602 nm emission associated with the $^1D_2 \rightarrow {}^3H_4$ transition is weak in the studied molybdate, whereas the $^3P_0$-related emissions at 490, 621, and 651 nm are dominant. Similar phenomena have been observed in other luminophores, such as PMN-PT:Pr^{3+} and La_2MgTiO_6:Pr^{3+}.[34,35] A simplified diagram of the Pr^{3+} energy levels is shown in the Fig. 4(b).

The quantum yield provides valuable insights into the optical performance of phosphors. The quantum yield (QY) of the CDs was determined using the integrating sphere method, which allows for an absolute measurement by directly quantifying both the emitted and absorbed photons. The general equation is as follows:

$$QY = \text{number of photons emitted/number of photons absorbed}$$

Fig. S_4† presents the curve of the absolute quantum yield measured using an integrating sphere. A quantum yield of 75% was observed for the studied, demonstrating its exceptional optical efficiency. Furthermore, the quantum yield of our analyzed phosphor exceeds that of several other commercial phosphors, such as Ca_2GdSbO_6:Eu^{3+} (73%),[36] Pr^{3+}-doped CAS glasses (37%),[37] GCs:Pr^{3+}/Yb^{3+} (38.9%)[38] and $Bi_4Si_3O_{12}$:Eu^{3+} (14.5%).[39]

In order to demonstrate ideal light qualities in the host under study findings, various concentrations of Pr^{3+} ions were doped into the host material, and their emission properties were examined. PL emission spectra at room temperature for different concentrations of Pr^{3+} ions doped into NCYM are shown in Fig. 5(a) NCYM:xPr^{3+} (x = 0.1, 0.2, 0.3 and 0.4), which shows only the emission bands of note for Pr^{3+} ions, and their intensities are controlled by the doping concentration at 450 nm excitation.

The photoluminescence (PL) intensity is observed to increase to 0.3 and subsequently decrease, as depicted in Fig. 5(a), due to the process of concentration quenching. Typically, concentration quenching occurs through one of two mechanisms: exchange interaction or electric multipolar interaction. Exchange interaction occurs when the wave functions of acceptor and donor ions overlap within a defined critical distance (R_C). This overlap reduces the intensity of emission peaks and increases nonradiative energy transfer between the ions. The critical distance between the two Pr^{3+} ions present in the NCYM lattice is calculated.[40–42]

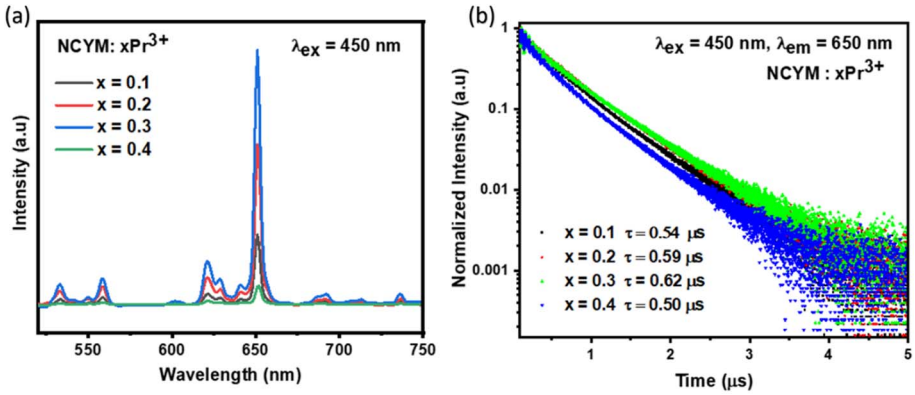

Fig. 5 (a) Emission spectrum of NCYM:xPr^{3+} (x = 0.1, 0.2, 0.3 and 0.4) excited at 450 nm, (b) decay curves of the 650 nm emission for the samples with different Pr^{3+} concentrations under 450 nm excitation.

$$R_c = 2 \times \left[\frac{3V}{4\pi X_c Z}\right]^{1/3} \quad (5)$$

The formula for the critical distance for Pr^{3+} ions in NCYM arrays is estimated as R_c = 7.86 Å, demonstrating the presence of the electric multipole interaction.

The emission decay curves of lanthanide-activated phosphors were also analyzed, and the correlation between activator concentration, luminescence characteristics, and decay duration could strongly support concentration quenching during the energy migration process. Fig. 5(b) shows the logarithmic intensity decay curves of red emissions at 650 nm in NCYM:xPr^{3+} phosphors (x = 0.1, 0.2, 0.3, and 0.4) under 450 nm excitation. The observed emission at 650 nm corresponds to the $^3P_0 \rightarrow {}^3F_2$ transition of Pr^{3+}, confirming that the initial excited state for this luminescence is 3P0^3P_03P0. All the decay curves can be fitted by the following:[43]

$$I(t) = A_1 \exp\left(-\frac{t}{\tau_1}\right) + A_2 \exp\left(-\frac{t}{\tau_2}\right) + I_0 \quad (6)$$

$$\tau = \frac{A_1\tau_1^2 + A_2\tau_2^2}{A_1\tau_1 + A_2\tau_2} \quad (7)$$

where t is time, $I(t)$ is afterglow emission, A_1 and A_2 is constant, τ_1 and τ_2 is the decay time of the exponential components, respectively. The average afterglow decay time (τ) of the bi-exponential function can be calculated by eqn (6). As shown in the figure, we measured the decay curves of a series of samples containing different concentrations of Pr^{3+} to illustrate the mechanism of cross-relaxation. As the Pr^{3+} doping concentration increases, the time required for the $^3F_2$-excited state to return to its ground state varies. This behavior is attributed to the cross-relaxation mechanism between Pr^{3+} ions. The results show that the decay time of the $^3F_2$ level increases with the doping concentration, rising from 0.54 μs for x = 0.1 to 0.62 μs for x = 0.3. However, at a higher concentration (x = 0.4), the decay time decreases to 0.50 μs, suggesting that excessive Pr^{3+} concentration may intensify ion–ion interactions, thereby reducing the decay time. The other NCYM:Pr^{3+} decay parameters were summarized, as shown in Table 1.

Table 1 Decay parameters of NCYM:xPr^{3+} (x = 0,1, 0.2, 0.3 and 0.4)

Sample	A_1	τ_1 (μs)	A_2	τ_2 (μs)	τ (μs)
NCYM:0.1Pr^{3+}	0.61	0.35	0.43	0.69	0.54
NCYM:0.2Pr^{3+}	0.75	0.45	0.27	0.81	0.59
NCYM:0.3Pr^{3+}	0.71	0.45	0.25	0.88	0.62
NCYM:0.4Pr^{3+}	0.63	0.28	0.41	0.64	0.50

4.4. Temperature sensing

In order to determine the potential of the materials studied for optical temperature measurement, the high-temperature photoluminescence (PL) spectra of NCYM:0.3Pr^{3+} were recorded. Fig. 6 shows the PL spectra recorded from 298 K to 498 K under excitation at 450 nm. Thanks to the presence of different Pr^{3+} emission bands, especially those of the $^3P_0 \rightarrow {}^3H_4$, $^3P_1 \rightarrow {}^3H_5$, $^3P_0 \rightarrow {}^3H_5$ and $^3P_0 \rightarrow {}^3F_2$ transitions, the microcrystal obtained can act as optical temperature monitors, based on the light intensity ratio of these bands. The total intensity of luminescence decreases progressively with increasing temperature. Therefore, two fluorescence intensity ratio (FIR) patterns are used as temperature detection signals due to the marked differences in temperature dependence between the three emissions ($^3P_1 \rightarrow {}^3H_5$ and $^3P_0 \rightarrow {}^3H_5$ (FIR1)), and ($^3P_1 \rightarrow {}^3H_4$ and $^3P_0 \rightarrow {}^3F_2$ (FIR2)).

The integrated intensities of the three emissions in Fig. 7(a and b) show that the intensities of FIR1 and FIR2 increase monotonically with increasing temperature. The FIR of the two models can be deduced and expressed as follows:[44,45]

$$\mathrm{FIR} = A \exp\left(\frac{-\Delta E}{K_B T}\right) \quad (8)$$

where K_B is the Boltzmann constant, T is the absolute temperature, A, and ΔE are parameters related to the curve of FIR.

In order to quantitatively determine the sensitivity of the two modes for optical thermometry, it is very important to analyze the relative and absolute sensitivity of the sensor, which is the ratio of the variation of the FIR with temperature and can be defined as follows:[46,47]

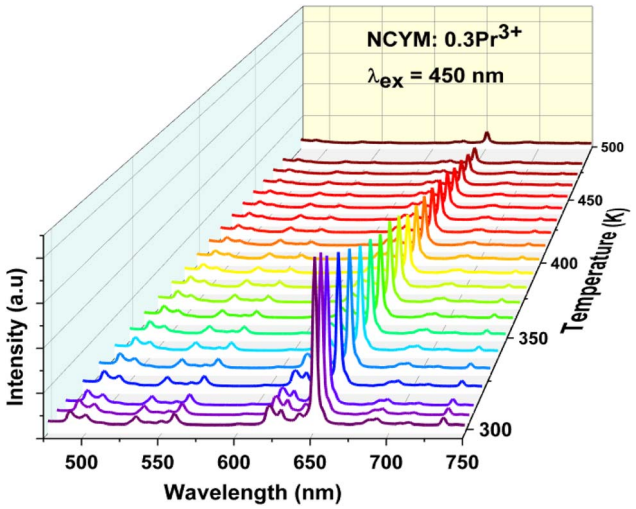

Fig. 6 Temperature dependence of the emission spectra of NCYM:0.3Pr^{3+} under 450 nm excitation.

$$S_r = \frac{1}{\mathrm{FIR}} \frac{\partial \mathrm{FIR}}{\partial T} \times 100\% \quad (9)$$

$$S_a = \frac{\partial \mathrm{FIR}}{\partial T} \quad (10)$$

The values of S_r and S_a, calculated by eqn (9) and (10), are shown in Fig. 8(a and b). The maximum S_r values for the models reach 0.69% per K and 1.2% per K at 298 K for FIR1 and FIR2, respectively. Similarly, the maximum S_a values reach 0.0054 per K (at 298 K) and 0.00085 per K (at 298 K) for FIR1 and FIR2, respectively. The NCYM:Pr^{3+} phosphors had three FIR models monitored. When one of the FIR patterns is in error, other patterns can be simultaneously monitored to correct the inaccuracy. In this way, the self-calibrating optical thermometer can be made by simultaneously monitoring two FIR patterns. To give the reader an idea of the current state of the art, a summary of the various luminescent thermometers based on the FIR technique is given in Table 2. It can be concluded that, compared with other works, our material offers superior performance.

Temperature resolution, also known as uncertainty (δT), is another key parameter that determines the smallest temperature change that can be detected by an optical thermometer and describes the possible error in temperature reading. The temperature uncertainty (δT) using luminescent thermometry can be calculated using the equation as follows:[57,58]

$$\delta T = \frac{1}{S_r} \frac{\delta \mathrm{FIR}}{\mathrm{FIR}} \quad (11)$$

In this study, the standard deviation of the fluorescence intensity ratio (δFIR) is defined as the variability of FIR values

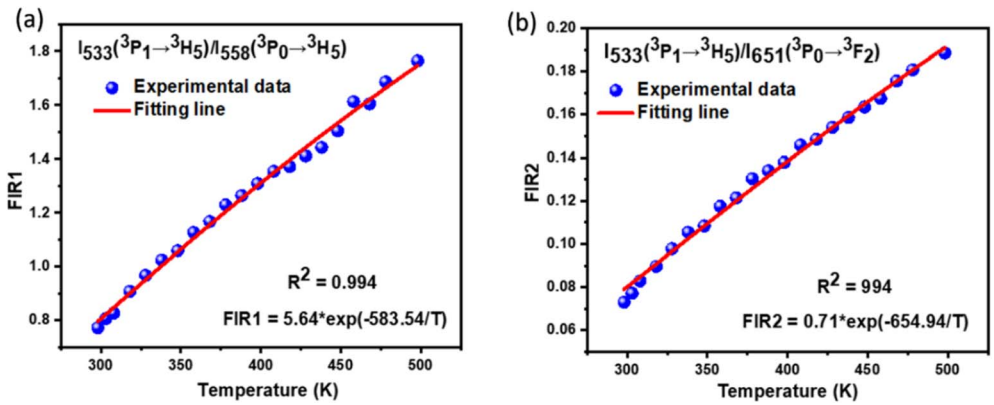

Fig. 7 (a and b) Variations of FIR as a function of temperature for NCYM:0.3Pr^{3+} between (a) ($^3P_1$–$^3H_5$/$^3P_0$–$^3H_5$), and (b) ($^3P_1$–$^3H_5$/$^3P_0$–$^3F_2$).

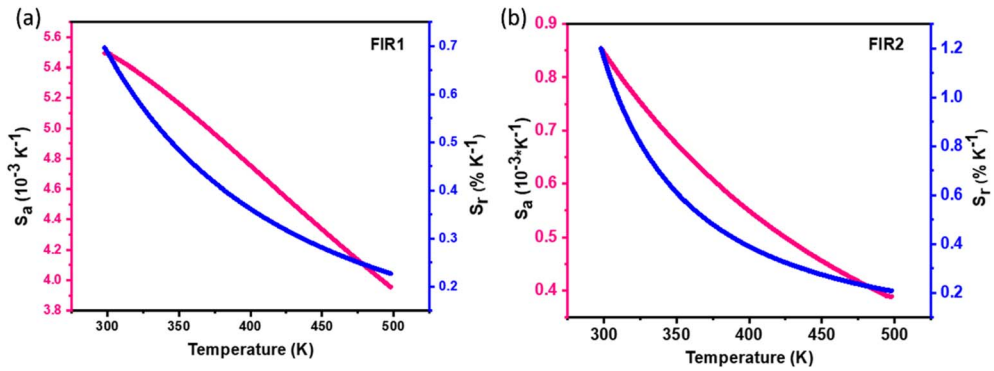

Fig. 8 (a and b) S_a and S_r values corresponding to (a) FIR1 ($^3P_1$–$^3H_5$/$^3P_0$–$^3H_5$), and (b) FIR2 ($^3P_1$–$^3H_5$/$^3P_0$–$^3F_2$).

Table 2 FIR-based thermometric performances of several typical Ln^{3+} ions doped materials

Materials	$S_{r\ max}$ (% per K)	T (K)	T-range (K)	Transitions	λ (nm)	Ref.
CaZnOS:Er^{3+}	0.33	603.15	303–603	$^2H_{11/2}/^4S_{3/2}$	520/539	48
PKAZLF glass:Er^{3+}	0.79	630	298–773	$^2H_{11/2}/^4S_{3/2}$	530/550	49
α-$NaYF_4$:Nd^{3+}	0.12	273	273–423	$^4F_{3/2}$–$^4I_{9/2}$ (Stark)	863/870	50
LaF_3:Nd^{3+}	0.26	296	296–345	$^4F_{3/2}$–$^4I_{9/2}$ (Stark)	865/885	51
β-$NaYF_4$:Yb^{3+}, Ho^{3+}	0.9	300	300–500	$^5F_5$–$^5I_8/^2S_2$, $^5F_4$–$^5I_8$	545/650	52
SrF_2:Yb^{3+}, Er^{3+}	1.20	298	298–383	$^2H_{11/2}/^4S_{3/2}$	525/545	53
β-$NaLuF_4$:Yb^{3+}, Er^{3+}, Ho^{3+}	0.74	298	298–503	$^2H_{11/2}/^4S_{3/2}$	527/547	54
$GdVO_4$:Er^{3+}/Yb^{3+}	0.7	300	300–453	$^2H_{11/2}/^4S_{3/2}$	530/550	55
$LaMgTiO_6$:Pr^{3+}	1.28	350	77–500	$^1D_2$, $^3P_0$–$^3H_4$	608/499	35
PMN-PT-PYN:Er^{3+}	0.3	—	113–413	$^2H_{11/2}/^4S_{3/2}$	525/539	56
PMN-PT:Pr^{3+}	0.70	—	223–313	$^3P_1$–$^3H_5/^3P_0$–$^3H_5$	534/500	34
PMN-PT:Pr^{3+}	0.06	—	223–313	$^3P_1$–$^3H_5/^3P_0$–$^3F_2$	534/650	34
NCYM:Pr^{3+}	0.69	298	298–498	$^3P_1$–$^3H_5/^3P_0$–$^3H_5$	533/558	**This work**
NCYM:Pr^{3+}	1.2	298	298–498	$^3P_1$–$^3H_5/^3P_0$–$^3F_2$	533/651	**This work**

obtained from repeated measurements at a constant temperature. The FIR itself represents the average value derived from these measurements. To establish the detection limit, 40 independent measurements were performed at room temperature under controlled conditions. The data are summarized in the histograms displayed in Fig. S_5(a and b).† The uncertainty in FIR (δFIR) was computed based on the statistical spread of the data for the NCYM:0.3Pr^{3+} sample, yielding values of 0.016 and 0.003 for FIR1 and FIR2, respectively. Using eqn (11), the corresponding temperature uncertainties (δT) were calculated and found to be below 0.06 K. These results highlight the high precision and reliability of the FIR-based models across the investigated temperature range.

This analysis underscores the exceptional temperature resolution of the NCYM phosphor. Specifically, the NCYM:0.3Pr^{3+} sample exhibits high thermal sensitivity coupled with minimal temperature measurement errors, making it a promising candidate for optical thermometry using the FIR method. The δT values for FIR1 and FIR2 are shown in Fig. 9(a and b), further demonstrating the robustness of this material in temperature sensing applications.

The repeatability (R) is another important way, to verify the accuracy of the temperature sensing techniques used. The thermometric parameters determined (FIR values) were measured repeatedly by moving the sample from a low temperature to a high temperature, as shown in Fig. 10(a and b). The calculation used to determine repeatability (R) was as follows:[59]

$$Rp(100\%) = \left(1 - \frac{\max\left|Mi(T)_c - M(T)_c\right|}{\mathrm{FIR}_c}\right) \times 100 \qquad (12)$$

where $Mi(T)_c$ is the measured parameter (FIR or band centroid) in the i^{th} cycle and $M(T)_c$ is the mean value of the $M(T)_c$ over 10 cycles. The FIR values determined change reversibly with temperature, and the FIR values for all FIRs were above 97% over the temperature range measured, confirming the good repeatability and reliability of the thermometric methods applied. Based on the above results, NCYM:0.3Pr^{3+} phosphor is a promising candidate for high-performance temperature sensing materials, as all two modes exhibit high temperature sensitivity as well as good resolution and repeatability.

4.5. Temperature-dependent color shifts and their implications for thermal sensing

The chromaticity diagram, along with the Commission Internationale de l'Éclairage (CIE) coordinates, offers a precise method for evaluating the emission color characteristics of luminescent

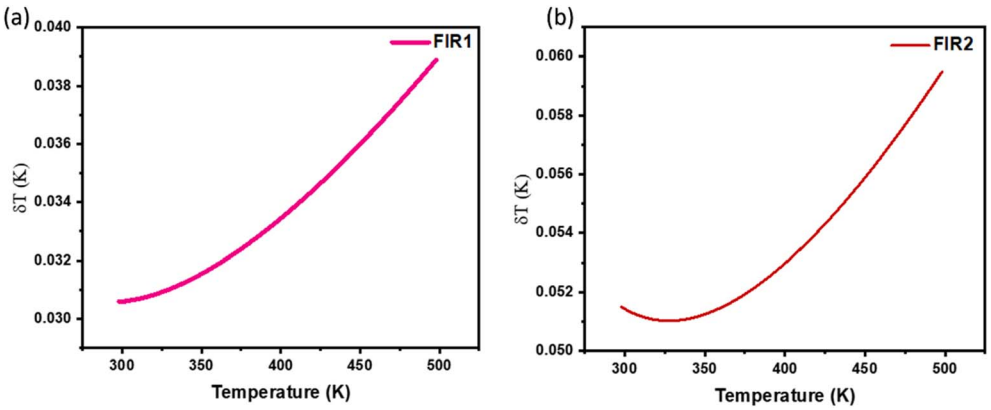

Fig. 9 (a and b) Temperature resolution values δT, corresponding to (a) FIR_2 ($^3P_1$–$^3H_5/^3P_0$–$^3H_5$) and (b) FIR_3 ($^3P_1$–$^3H_5/^3P_0$–$^3F_2$) for NCYM:0.3Pr^{3+}.

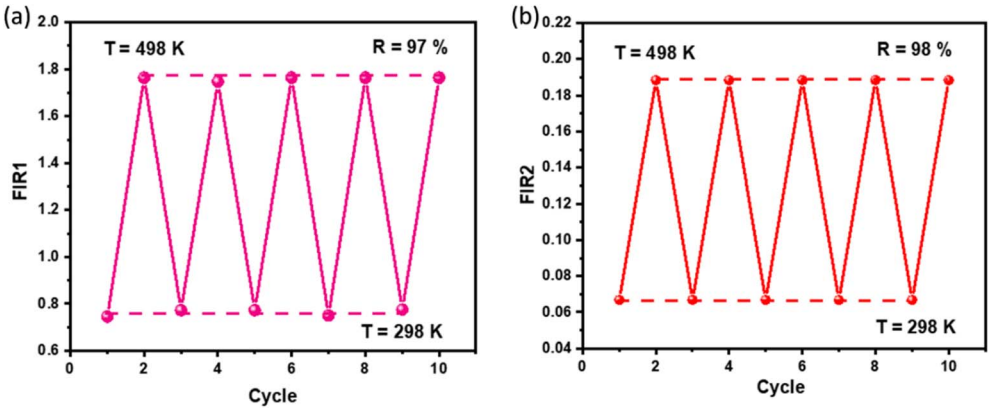

Fig. 10 Repeatability assessment (*R*) (a and b) for NCYM:0.3Pr^{3+}.

materials. In this study, the impact of temperature on the emission color of NCYM:0.3Pr^{3+} was systematically analyzed through CIE chromaticity coordinates, measured under 450 nm excitation across a temperature range from 298 K to 498 K. As depicted in Fig. 11, the CIE coordinates of the sample shift from ($x = 0.3806, y = 0.4278$) at 298 K to ($x = 0.3772, y = 0.4229$) at 498 K, indicating a clear and stable transition in emission color toward the yellow region as the temperature increases. The change in the x and y values reflects the continuous and stable shift in emission towards yellow, which occurs as a result of the thermal activation of different electronic states in the Pr^{3+} ions.

This color shift provides critical insights into the temperature-dependent behavior of the material, suggesting that NCYM:0.3Pr^{3+} could be employed as a visual thermal sensor. The color change is stable and consistent over the studied temperature range, which is a crucial characteristic for practical thermal safety applications. Unlike traditional temperature sensors, which rely on electronic measurements, the color shift observed here offers an optical, non-contact alternative for temperature monitoring, making it suitable for environments where conventional sensors may be impractical.

The observed temperature-induced color shift is attributed to the thermal population of different electronic states in the Pr^{3+} ion, specifically the $^3P_0$ and $^3P_1$ states, which are responsible for the observed visible emissions. The correlation between temperature and emission color could thus be exploited for real-time monitoring of temperature fluctuations. This feature enhances the material's potential as a thermal safety indicator, where rapid visual detection of temperature variations could serve as an early warning system in sensitive applications, such as in electronics, automotive, or aerospace industries.

Additionally, the stable shift in CIE coordinates towards yellow over the entire temperature range suggests that NCYM:0.3Pr^{3+} can be a versatile material for applications requiring continuous monitoring or dynamic color changes with temperature. The gradual shift across the chromaticity diagram could be utilized in color-based thermal imaging systems, offering a straightforward method for visualizing temperature distributions. The precise CIE coordinates at room temperature (298 K) of ($x = 0.3806, y = 0.4278$) and at 498 K of ($x = 0.3772, y = 0.4229$) confirm that the material's emission color transitions in a controlled, repeatable manner, making it a reliable choice for real-time thermal imaging applications.

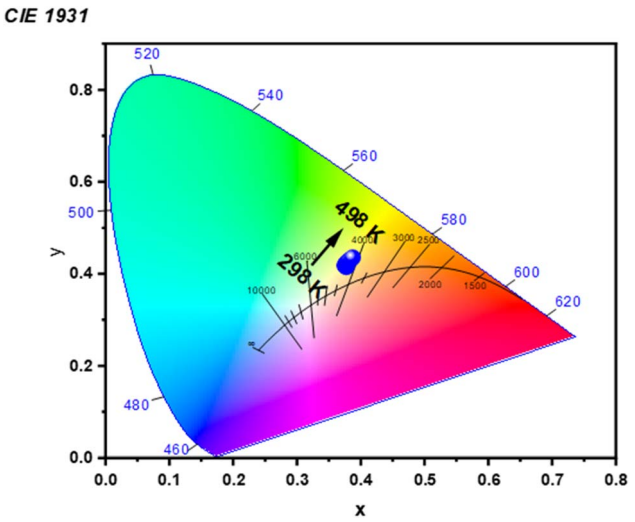

Fig. 11 CIE (*x*,*y*) coordinate diagram of the emission color at different temperature for NCYM:0.3Pr^{3+}.

5. Conclusion

In summary, Pr^{3+}-doped NCYM luminophores, synthesized using the citrate-based sol–gel method, demonstrate significant potential for advanced optical applications. The scheelite-type tetragonal structure with space group $I4_1/a$ was confirmed by XRD and Rietveld refinement analysis. SEM analysis revealed an average particle size of approximately 3 μm. Absorption measurements revealed the molybdate host's characteristic absorption band in the visible region. The optical band gap (3.36–3.84 eV) showed minimal impact from Pr^{3+} doping on the host's electronic structure. Photoluminescence spectra under 450 nm excitation exhibited strong cyan, green, and red emissions, with optimal luminescence achieved at a 0.3 mol% doping concentration. These microparticles displayed excellent potential as optical, non-

contact temperature sensors, with temperature-dependent emission intensity ratios yielding high sensitivity (0.69, and 1.2% per K for 533/558, and 533/651 nm ratios, respectively). Luminescence thermometry demonstrated impressive precision, with temperature uncertainty (δT) below 0.06 K and repeatability over 97%. Additionally, the temperature-induced chromaticity shift further enhances the material's functionality, as the CIE coordinates shifted from (0.3806, 0.4278) at 298 K to (0.3772, 0.4229) at 498 K, indicating a stable transition toward yellow. This highlights NCYM:0.3Pr^{3+} as a promising candidate for practical thermal indicators and sensors in high-precision, non-contact temperature measurements. Overall, the superior accuracy and reliability of Pr^{3+}-doped NCYM as an optical thermometer position it for transformative applications in precision temperature monitoring, thermal management, and safety systems. This work lays the groundwork for future advancements in optical thermometry.

Data availability

All data underlying the results are available as part of the article and no additional source data are required.

Conflicts of interest

There are no conflicts to declare.

References

1 X. Wang, O. S. Wolfbeis and R. J. Meier, Luminescent probes and sensors for temperature, *Chem. Soc. Rev.*, 2013, **42**, 7834–7869.
2 M. D. Dramićanin, Sensing temperature *via* downshifting emissions of lanthanide-doped metal oxides and salts. A review, *Methods Appl. Fluoresc.*, 2016, **4**, 042001.
3 J. Zhong, *et al.*, A review on nanostructured glass ceramics for promising application in optical thermometry, *J. Alloys Compd.*, 2018, **763**, 34–48.
4 K. Saidi, C. Hernández-Álvarez, M. Runowski, M. Dammak and I. R. Martín, Ultralow pressure sensing and luminescence thermometry based on the emissions of Er^{3+}/Yb^{3+} codoped $Y_2Mo_4O_{15}$ phosphors, *Dalton Trans.*, 2023, **52**, 14904–14916.
5 M. Quintanilla, M. Henriksen-Lacey, C. Renero-Lecuna and L. M. Liz-Marzán, Challenges for optical nanothermometry in biological environments, *Chem. Soc. Rev.*, 2022, **51**, 4223–4242.
6 K. Saidi, I. Kachou, K. Soler-Carracedo, M. Dammak and I. R. Martín, $Ba_2YV_3O_{11}$ Er^{3+}/Yb^{3+} Nanostructures for Temperature Sensing in the Presence of Bismuth Ions, *ACS Appl. Nano Mater.*, 2023, **6**, 17681–17690.
7 Z. Wang, *et al.*, Nd^{3+} -sensitized $NaLuF_4$ luminescent nanoparticles for multimodal imaging and temperature sensing under 808 nm excitation, *Nanoscale*, 2015, **7**, 17861–17870.
8 S. Zheng, *et al.*, Lanthanide-doped $NaGdF_4$ core–shell nanoparticles for non-contact self-referencing temperature sensors, *Nanoscale*, 2014, **6**, 5675–5679.
9 W. Xu, *et al.*, Optical temperature sensing through the upconversion luminescence from Ho^{3+}/Yb^{3+} codoped $CaWO_4$, *Sens. Actuators, B*, 2013, **188**, 1096–1100.
10 D. Chen, *et al.*, Dual-activator luminescence of RE/TM:$Y_3Al_5O_{12}$ (RE = Eu^{3+}, Tb^{3+}, Dy^{3+}; TM = Mn^{4+}, Cr^{3+}) phosphors for self-referencing optical thermometry, *J. Mater. Chem. C*, 2016, **4**, 9044–9051.
11 Z. E. A. A. Taleb, K. Saidi and M. Dammak, Dual-mode optical ratiometric thermometry using Pr^{3+}-doped $NaSrGd(MoO_4)_3$ phosphors with tunable sensitivity, *Dalton Trans.*, 2023, **52**, 18069–18081.
12 K. Saidi and M. Dammak, Upconversion luminescence and optical temperature sensing characteristics of Er^{3+}/Yb^{3+} codoped $Na_3Gd(PO_4)_2$ phosphors, *J. Solid State Chem.*, 2021, **300**, 122214.
13 M. Yangui, K. Saidi, C. Hernández-Álvarez, M. Dammak and I. R. Martín, Ratiometric luminescent thermometry with excellent sensitivity in the visible and near-infrared (NIR-II/III) based on thermally coupled and non-thermally coupled energy levels of Er^{3+} and Ho^{3+} ions, *J. Alloys Compd.*, 2025, **1010**, 177958.
14 C. Hernández-Álvarez, *et al.*, Multifunctional optical sensing platform of temperature, pressure (vacuum) and laser power density:$NaYF_4$:Gd^{3+}, Yb^{3+}, Er^{3+} nanomaterial as luminescent thermometer, manometer and power meter, *J. Mater. Chem. C*, 2023, **11**, 10221–10229.
15 I. Kachou, K. Saidi, C. Hernández-Álvarez, M. Dammak and I. R. Martín, Enhancing thermometric precision: modulating the temperature of maximum sensitivity *via* erbium dopant addition in $Ba_2GdV_3O_{11}$:Tm^{3+}/Yb^{3+} nano phosphors, *Mater. Adv.*, 2024, **5**, 8280–8293.
16 W. Xu, X. Gao, L. Zheng, Z. Zhang and W. Cao, An optical temperature sensor based on the upconversion luminescence from Tm^{3+}/Yb^{3+} codoped oxyfluoride glass ceramic, *Sens. Actuators, B*, 2012, **173**, 250–253.
17 D. Chen, *et al.*, Bulk glass ceramics containing Yb^{3+}/Er^{3+}: β-$NaGdF_4$ nanocrystals: Phase-separation-controlled crystallization, optical spectroscopy and upconverted temperature sensing behavior, *J. Alloys Compd.*, 2015, **638**, 21–28.
18 R. A. Talewar, V. M. Gaikwad, P. K. Tawalare and S. V. Moharil, *Opt Laser. Technol.*, 2019, **115**, 215–221.
19 L. Li, P. Yang, W. Xia, Y. Wang, F. Ling, Z. Cao, S. Jiang, G. Xiang, X. Zhou and Y. Wang, *Ceram. Int.*, 2021, **47**, 769–775.
20 Y. Bahrouni, I. Kachou, K. Saidi, T. Kallel, M. Dammak, I. Mediavilla and J. Jiménez, *Mater. Adv.*, 2025, advance (in press).
21 L. Li, P. Yang, W. Xia, Y. Wang, F. Ling, Z. Cao, S. Jiang, G. Xiang, X. Zhou and Y. Wang, *Ceram. Int.*, 2021, **47**, 769–775.
22 J. Wang, N. Chen, J. Li, Q. Feng, R. Lei, H. Wang and S. Xu, *J. Lumin.*, 2021, **238**, 118240.
23 M. Enneffati, M. Rasheed, B. Louati, K. Guidara and R. Barillé, *Opt. Quantum Electron.*, 2019, **51**, 299.
24 K. Baishya, J. S. Ray, P. Dutta, P. P. Das and S. K. Das, *Appl. Phys. A*, 2018, **124**, 704.

25 Y. Gao, F. Huang, H. Lin, J. Xu and Y. Wang, *Sens. Actuators, B*, 2017, **243**, 137–143.
26 M. Fhoula, K. Saidi, C. Hernández-Álvarez, K. Soler-Carracedo, M. Dammak and I. R. Martín, *J. Alloys Compd.*, 2024, **979**, 173537.
27 K. Saidi, M. Yangui, C. Hernández-Álvarez, M. Dammak, I. Rafael Martín Benenzuela and M. Runowski, *ACS Appl. Mater. Interfaces*, 2024, **16**, 19137–19149.
28 M. J. Weber, Multiphonon Relaxation of Rare-Earth Ions in Yttrium Orthoaluminate, *Phys. Rev. B*, 1973, **8**, 54–64.
29 S. A. Payne and C. Bibeau, Picosecond nonradiative processes in neodymium-doped crystals and glasses, *J. Lumin.*, 1998, **79**, 143–159.
30 M. V. V. Kumar, K. R. Gopal, R. R. Reddy, G. V. L. Reddy, N. S. Hussain and B. C. Jamalaiah, *J. Non-Cryst. Solids*, 2013, **364**, 20–27.
31 V. Naresh and B. S. Ham, *J. Alloys Compd.*, 2016, **664**, 321–330.
32 H. Dornauf and J. Heber, *J. Lumin.*, 1980, **22**, 1–16.
33 C. De Mello Donegá, A. Meijerink and G. Blasse, *J. Phys. Chem. Solids*, 1995, **56**, 673–685.
34 Y. Qin, *et al.*, Fluorescence intensity ratio (FIR) analysis of the temperature sensing properties in transparent ferroelectric PMN-PT:Pr^{3+} ceramic, *Ceram. Int.*, 2021, **47**, 24092–24097.
35 R. Shi, L. Lin, P. Dorenbos and H. Liang, Development of a potential optical thermometric material through photoluminescence of Pr^{3+} in La_2MgTiO_6, *J. Mater. Chem. C*, 2017, **5**, 10737–10745.
36 Z. Zhang, L. Sun, B. Devakumar, J. Liang, S. Wang, Q. Sun, S. J. Dhoble and X. Huang, *J. Lumin.*, 2020, **221**, 117105.
37 C. Y. Morassuti, *et al.*, Spectroscopic investigation and interest of Pr^{3+}-doped calcium aluminosilicate glass, *J. Lumin.*, 2019, **210**, 376–382.
38 D. Ding, J. Gao, S. Zhang and L. Duo, The photoluminescence properties of Pr^{3+}-Yb^{3+} co-doped gallo-germanate glasses and glass ceramics as energy converter, *J. Lumin.*, 2020, **226**, 117512.
39 J. Y. Park, S. J. Park and H. K. Yang, Investigation of red-emitting $Bi_4Si_3O_{12}$:Eu^{3+} phosphor under the deep UV irradiation as a novel material for white light and color tunable emission, *Optik*, 2018, **166**, 69–76.
40 K. Saidi, W. Chaabani and M. Dammak, Highly sensitive optical temperature sensing based on pump-power-dependent upconversion luminescence in $LiZnPO_4$:Yb^{3+}–Er^{3+}/Ho^{3+} phosphors, *RSC Adv.*, 2021, **11**, 30926–30936.
41 I. Kachou, K. Saidi, R. Salhi and M. Dammak, Synthesis and optical spectroscopy of Na_3 $Y(VO_4)_2$:Eu^{3+} phosphors for thermometry and display applications, *RSC Adv.*, 2022, **12**, 7529–7539.
42 Z. E. A. A. Taleb, K. Saidi and M. Dammak, The dual-model up/down-conversion green luminescence of $NaSrGd(MoO_4)_3$:Er^{3+} and its application for temperature sensing, *RSC Adv.*, 2024, **14**, 8366–8377.
43 J. Wang, N. Chen, J. Li, Q. Feng, R. Lei, H. Wang and S. Xu, *J. Lumin.*, 2021, **238**, 118240.
44 J. Xing, F. Shang and G. Chen, *Ceram. Int.*, 2021, **47**, 8330–8337.
45 L. Li, P. Yang, W. Xia, Y. Wang, F. Ling, Z. Cao, S. Jiang, G. Xiang, X. Zhou and Y. Wang, *Ceram. Int.*, 2021, **47**, 769–775.
46 Z. E. A. A. Taleb, K. Saidi, M. Dammak, D. Przybylska and T. Grzyb, Ultrasensitive optical thermometry using Tb^{3+} doped NaSrGd(MoO4)3 based on single band ratiometric luminescence, *Dalton Trans.*, 2023, **52**, 4954–4963.
47 X. Zhou, *et al.*, Tunable emission color of Li_2SrSiO_4:Tb^{3+} due to cross-relaxation process and optical thermometry investigation, *J. Am. Ceram. Soc.*, 2018, **101**, 3076–3085.
48 H. Zhang, D. Peng, W. Wang, L. Dong and C. Pan, Mechanically Induced Light Emission and Infrared-Laser-Induced Upconversion in the Er-Doped CaZnOS Multifunctional Piezoelectric Semiconductor for Optical Pressure and Temperature Sensing, *J. Phys. Chem. C*, 2015, **119**, 28136–28142.
49 N. Vijaya, *et al.*, Optical characterization of Er^{3+}-doped zinc fluorophosphate glasses for optical temperature sensors, *Sens. Actuators, B*, 2013, **186**, 156–164.
50 D. Wawrzynczyk, A. Bednarkiewicz, M. Nyk, W. Strek and M. Samoc, Neodymium (III) doped fluoride nanoparticles as non-contact optical temperature sensors, *Nanoscale*, 2012, **4**, 6959–6961.
51 L. Marciniak, A. Pilch, S. Arabasz, D. Jin and A. Bednarkiewicz, Heterogeneously Nd^{3+} doped single nanoparticles for NIR-induced heat conversion, luminescence, and thermometry, *Nanoscale*, 2017, **9**, 8288–8297.
52 H. Li, Y. Zhang, L. Shao, Z. Htwe and P. Yuan, Luminescence probe for temperature sensor based on fluorescence intensity ratio, *Opt. Mater. Express*, 2017, **7**, 1077–1083.
53 S. Balabhadra, M. L. Debasu, C. D. S. Brites, R. A. S. Ferreira and L. D. Carlos, Upconverting Nanoparticles Working As Primary Thermometers In Different Media, *J. Phys. Chem. C*, 2017, **121**, 13962–13968.
54 N. Niu, *et al.*, Tunable multicolor and bright white emission of one-dimensional NaLuF4:Yb3+, Ln3+ (Ln = Er, Tm, Ho, Er/Tm, Tm/Ho) microstructures, *J. Mater. Chem.*, 2012, **22**, 10889.
55 J. Postlethwait, *et al.*, Correction: Vertebrate genome evolution and the zebrafish gene map, *Nat. Genet.*, 1998, **19**, 303.
56 J. Zhu, *et al.*, Improving the up/down-conversion luminescence *via* cationic substitution and dual-functional temperature sensing properties of Er^{3+} doped double perovskites, *Chem. Eng. J.*, 2023, **471**, 144550.
57 M. Rajendran and S. Vaidyanathan, High performance red/deep-red emitting phosphors for white LEDs, *New J. Chem.*, 2020, **44**, 5354–5365.
58 M. S. Pudovkin, O. A. Morozov, V. V. Pavlov, S. L. Korableva, E. V. Lukinova, Y. N. Osin, V. G. Evtugyn, R. A. Safiullin and V. V. Semashko, Physical Background for Luminescence Thermometry Sensors Based on Pr^{3+}:LaF_3 Crystalline Particles, *J. Nanomater.*, 2017, **2017**(1), 3108586.
59 A. Ćirić, *et al.*, Comparison of three ratiometric temperature readings from the Er^{3+} upconversion emission, *Nanomaterials*, 2020, **10**, 627.